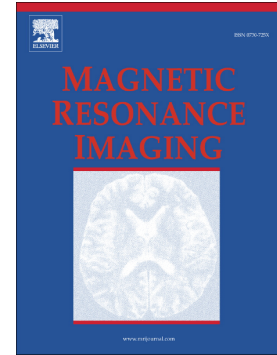# Accepted Manuscript

A Fully Automated Method for Accurate Measurement of Geometrical Distortion in Magnetic Resonance Imaging of a 3D-Lattice Phantom

S. Mangione, R. Acquaviva, G. Garbo

Please cite this article as: S. Mangione, R. Acquaviva, G. Garbo , A Fully Automated Method for Accurate Measurement of Geometrical Distortion in Magnetic Resonance Imaging of a 3D-Lattice Phantom. Mri (2018), https://doi.org/10.1016/j.mri.2018.10.011

A Fully Automated Method for Accurate Measurement of Geometrical Distortion in Magnetic Resonance Imaging of a 3D-Lattice Phantom

S. Mangione[a,b], R. Acquaviva[a], G. Garbo[a,b]

[a]*Università degli Studi di Palermo*
Dipartimento dell'Energia, Ingegneria dell'Informazione e Modelli Matematici
[b]*Consorzio Nazionale Interuniversitario per le Telecomunicazioni*

Abstract

This paper describes an automated method for extracting the apparent positions of fiducial points from 2D or 3D images of a phantom. We consider a 3D-lattice phantom for two main reasons: first, ease of manufacture and isotropy of its structure with respect to coordinate projections; second, a connected structure allowing to uniquely assess the adjacency relationship between fiducial points even if geometric distortions arising from main magnet inhomogeneity and gradient fields non-linearity is severe as observed in open-bore systems.

In order to validate our proposed method and compare different choices for the parameters of our phantom (i.e. number and distance between grids and thickness of its branches) we developed in-house a software for simulating 2D or 3D volume images of the phantom, using customizable MRI sequence parameters and Spherical Harmonic Coefficients for the fields.

We deem worthy of note that using simulated images is the only way to evaluate the estimated position error, since it allows to compare the estimates to their theoretical counterparts. Furthermore, the use of simulated images allows to evaluate the robustness of the method with respect to image quality in terms of Signal-to-Noise Ratios and geometric distortion, and allows to evaluate different phantom geometries without having to manufacture them. The proposed method can be easily extended to phantoms having an arbitrary overall shape, as long as it is a fully connected structure. Specifically, it is easy to design a phantom with fiducial points laying outside of the homogeneity sphere, so that indirect measurement of the fields becomes possible, for example by using the recent method proposed by Acquaviva *et al.*

To the best of our knowledge, the proposed method outperforms other state-of-the-art methods, with an average positioning offset of 0.052 mm (with a 0.99 quantile of 0.12 mm) when working on images featuring a differential Signal-to-Noise Ratio within Region-of-Interest (ROI) equal to 105 (20.2 dB) and a ROI-to-background SNR of 20 dB. Estimating the positions of 6859 fiducial points

---

in a volume, our highest density case, was carried out in less than 30 minutes on a desktop personal computer.

1. Introduction

Magnetic Resonance Imaging is affected by geometrical distortion due to magnetic field inhomogeneity and gradient non linearity. Magnetic field inhomogeneity in modern MRI systems is usually observable in permanent magnet and/or open bore systems, while gradient non linearity is usually due to engineering trade-offs in gradient coil design. Both distortion types are usually corrected via software, by using vendor-provided Spherical Harmonics Coefficients (SHC) sets that describe the fields within a so-called homogeneity sphere. The reason for using a sphere is that the SHC expansion is relatively easy to obtain by measuring precession frequencies of a number of probes placed at a given radius from the magnet isocentre. The diameter of the measurement sphere is limited by the magnet bore width, and it is well known that a spherical harmonic expansion cannot be extrapolated outside of its reference radius. Images acquired from planes laying partially outside of the homogeneity sphere usually show increased distortion that cannot be corrected by vendor-provided sets, and eventually exhibit signal loss due to precession frequencies outside of the receiver bandwidth.

On the basis of the fact that the fields vary continuously in space, and that the signal loss usually happens at much larger radii than the reference radius, a recent paper by Aquaviva et al [1] describes how to obtain a set of SHC's valid outside of the homogeneity sphere, as long as the distortion is observable and no aliasing effects occur. The method is based on reliable estimates of the positions of a large number (e.g. in the order of thousands) of fiducial points within the imaging volume.

Several papers deal with MRI phantoms specifically designed for fiducial point localization [2–4]. Accurate fiducial point localization in space is also essential for surgery and radio-therapy planning. The phantom proposed by Wang [2] is a Z-directed array of X-Y fin grids immersed in an MR-visible solution. They compute the Z-direction derivative and extract fiducial point positions by correlating to a 2D cross-prototype.

Huang *et al* [3] underlines that Wang's *et al* method is impaired in the low-SNR regime, since noise effects are worsened by the derivative, and when geometric-distortion induces intensity variations high enough to make a fixed threshold for fiducial point detection unreliable. They propose a phantom built as a 3D array of spheres full of contrast solution. The spherical shape has been chosen for being relatively insensitive to geometrical distortion, and fiducial point locations are found by searching maxima of normalized cross-covariance

2

between vendor-provided geometrically corrected images and a sphere prototype. More recently, Weavers *et al* [4] devised a similar method based on a phantom made of MR-visible spheres (water-based paintballs) arranged in a 3D grid of foam sheets. They acquire a CT scan of the phantom to set the ground truth, then iteratively match the entire distorted volume deriving SHC expansions of the fields as a result.

Both of these more recent methods employ spheres in order to simplify locating fiducial points, but this choice makes it cumbersome to derive their adjacency relationship[2] when geometrical distortion is significant. Weavers' approach overcomes this problem by matching the entire volume, but this results in a very heavy computational burden. Huang works with geometrically corrected images so the adjacency relationship issue is trivially solved.

The objective of the present work is to determine the apparent positions and adjacency relationship of a large number of fiducial points in raw images affected by geometrical distortion. To this purpose, we use a 3D lattice phantom of cylinders filled with an MR-visible solution. We consider the positions of 3D crosses as fiducial points. Their localization is carried out by searching maxima of the cross covariance between images and 3D cross prototypes. To overcome the geometrical distortion issue pointed out by [3, 4], and in order to be able to work on raw images, we employ 3D cross prototypes that are adaptive, i.e. determined on the basis of local features of the images themselves. In fact, we will show how it is possible to find the apparent directions of phantom features from geometrically distorted images without necessarily know the accurate positions of crosses. These directions will enable us to build 3D cross-prototypes on-the-fly, and determine the adjacency relationship between fiducial points in images. This aspect of the problem has, to the best of our knowledge, been neglected in the literature.

Once the apparent positions of fiducial points and their adjacency relationship is known, it becomes possible to apply the algorithm reported in [1] for estimation of Spherical Harmonic Coefficients. Note that the estimated SHC sets provide a valid field expansion within the volume enclosed by the envelope of the fiducial points whose positions have been determined, in particular also outside of the homogeneity sphere, as long as the corresponding fiducial points are observable and distinguishable.

In order to assess the validity of the proposed method, after evaluation of a real phantom having a similar structure, we chose to use simulated images. To the best of our knowledge, available MRI image simulators are voxel-based and focused on accurate simulation of the Bloch equation. This kind of simulator could not be used for our purposes, i.e. sub-voxel feature localization, so we decided to implement in-house an *ad-hoc* simulator. Our simulator is inspired by Monte-Carlo integration [5]. Specifically, instead of using a voxel-based dis-

---

[2]In the context of this paper, the adjacency relationship is a table stating the correspondence between a fiducial point in the phantom and its apparent position in the imaging volume. For a 3D grid phantom, every fiducial point can be easily identified by three integers.
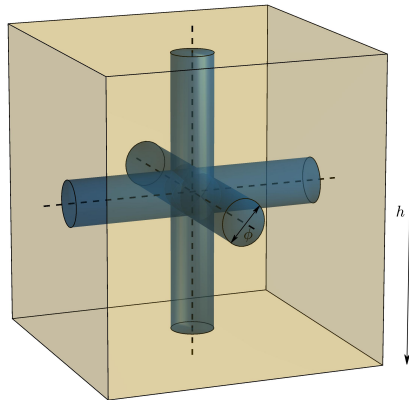
3

Figure 1: The elementary structure (*cross*) of which the phantom is made. A fiducial point (*node*) is located in the center.

cretization of the imaging volume, our model consists in generation of a set of random points (drawn within the phantom geometry) whose density determines the differential Signal-to-Noise Ratio of images, while yielding a very high ROI-to-background SNR that can be adjusted by adding thermal noise. Other simulation parameters include phantom geometry, the truncated Spherical Harmonics Expansions of the fields, and 2D Spin Echo or 3D Gradient Echo MRI sequence parameters. The simulator is focused on reproducing the geometrical distortion effects arising from main magnet field inhomogeneity and gradient fields non-linearities, and will yield accurate images as long as the susceptibility effects are negligible.

The paper is organized as follows. Section 2 describes the proposed phantom geometry, detailing its parameters, and shows some real acquired images in comparison to simulated images. Section 3 and its five subsections deal with the iterative method we developed in order to obtain the fiducial point positions and their adjacency relationship. Section 4 reports about the performance evaluation we conducted and the impact of phantom geometry settings and of Signal-to-Noise Ratios. A comparison to the fiducial point locating method proposed by Huang *et al* [3] is also reported. Section 5 draws conclusions and pointers for future works.

## 2. Phantom geometry and image acquisition

Our phantom may be described as the juxtaposition of elementary objects, called *crosses* in the following, made from three mutually-orthogonal cylinders of length h and diameter ϕ, whose axes meet in the middle, as shown in Fig. 1. The centre of each cross constitutes our fiducial point and will be called *node* from here onwards. The active volume of the phantom will be a connected set of crosses filled with MR-visible solution, and may assume an arbitrary overall shape. For simplicity we adopted a regular lattice inscribed in a parallelepiped,
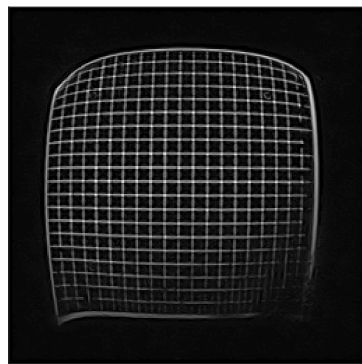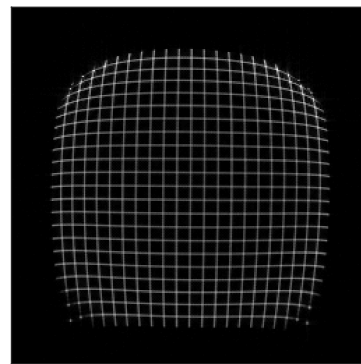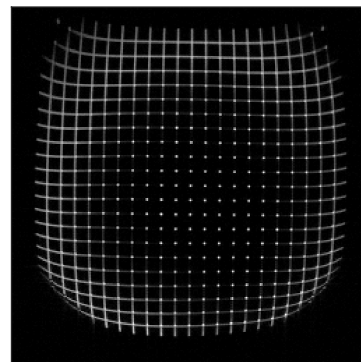
4

(a) Raw image at isocentre

(b) Simulated image at isocentre
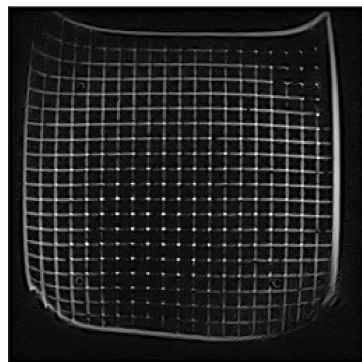
(c) Raw image at 60 mm from isocentre   (d) Simulated image at 60 mm from isocentre

Figure 2: Geometric distortion in 2D SE real and simulated images of a 3D grid phantom

so that each node can be uniquely identified by a triad of indices (row, column, slice). Each cross features six *branches* having length $h/2$, and will be connected to up to six other crosses within the phantom. The proposed structure, to be filled with MR-visible solution, may be manufactured by 3D printing, or superposition of CNC-milled acrylic sheets.

In order to validate our method, we developed in-house an MRI image simulator. Our simulator is inspired by Monte-Carlo integration with a user-input spatial point density, and can compute the Free Induction Decay signal of 2D Spin Echo or 3D Gradient Echo sequences. The expression we used for computing the 3D FID is Eq. (10) from [6], and was approximated as

$$S_{\text{GE}}(k_x, k_y, k_z) \approx \sum_n e^{-j2\pi(k_x(x_n + \frac{\Delta B}{G_x}) + k_y y_n + k_z z_n)} \tag{1}$$

where the points (x_n, y_n, z_n) are randomly selected from the MR-visible volume. The simulator requires the SHC expansion of both static and gradient fields, MRI sequence parameters, and a mathematical description of the MR-visible volume geometry.

We evaluated both the ROI-to-background and the differential [7] Signal-to-Noise Ratio of simulated images. Both directly depend on the user-input spatial point density. Obviously, a minimum density is required in order to form images, and we found that, in this case, the ROI-to-background[3] Signal-to-Noise Ratio always results higher than 40 dB (i.e. 10000). Lower ROI-to-background SNR's can be obtained by adding a suitable noise model to the simulated Free Induction Decays. The differential SNR, defined as the ratio between the mean square of intensity and the variance of random fluctuations within a ROI, is substantially equal to the random point density times the volume of a voxel (i.e. it can be explained as a counting-error). Figure 3a shows the same ROI (an axial section of a cylinder filled with MR-visible solution) with several point densities along with their estimated differential SNR. Figure 3b provides a similar comparison from the point-of-view of ROI-to-background SNR. Note that the ROI is barely discernible at a ROI-to-background SNR of 3 dB.

In order to obtain realistic images, we used vendor-provided SHC sets for an open-bore 0.3 T C-shaped permanent magnet MRI system featuring an homogeneity sphere diameter equal to 250 mm. The geometric distortion outside of the homogeneity sphere, i.e. in slices far from the magnet isocentre, is clearly observable. Figure 2 shows some real uncorrected 2D Spin Echo images of a grid phantom prototype that was available in the early stage of our work, similar in design to the one described above. The same figure also includes simulated images obtained using the same sequence parameters, with a spatial point density of 500 points/mm^3 and an additive thermal noise resulting in a ROI-to-background SNR of 43 dB. The phantom prototype has h=10 mm and ϕ=2 mm.

---

[3]we evaluate the ROI-to-background Signal-to-Noise Ratio as the ratio between the mean voxel intensity in the Region-of-Interest and the standard deviation of the background voxel intensity.

(a)

ROI-to-background Signal-to-Noise Ratio, dB
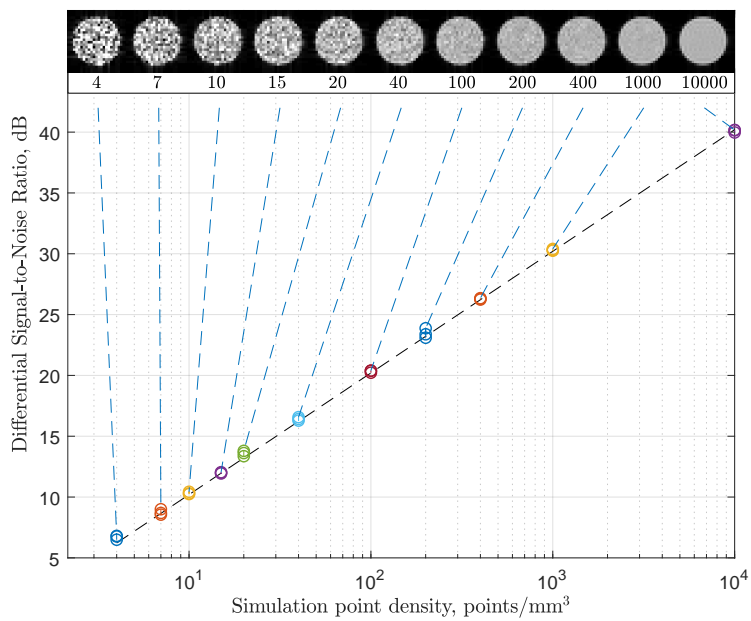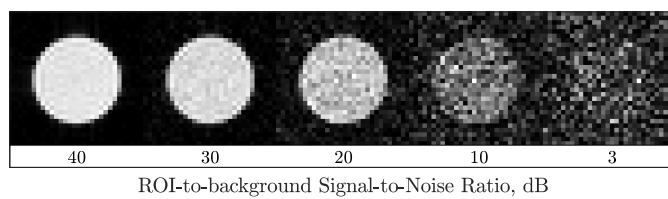
(b)

Figure 3: (a) Differential Signal-to-Noise Ratio as a function of simulation point density (b) ROI-to-background Signal-to-Noise Ratio (random gaussian noise)

The FOV is equal to 260 mm, and the resolution of images is $N^2 = 256 \times 256$ pixels. Geometric and through-plane distortions are clearly observable in slices distant 60 mm from the isocentre, while, as expected, are negligible for slices in the neighbourhood of the magnet isocentre.

In what follows, we consider simulated 3D Gradient Echo volumes with a FOV of 260 mm in each direction and a resolution of $N^3 = 256 \times 256 \times 256$ with isotropic voxels. Figure 4 shows some representative simulated images of a regular lattice phantom of $19 \times 19 \times 19$ nodes with $h{=}10$ mm, $\phi{=}3$ mm. The simulation was run with a random point density of 100 points/mm^3, resulting in a differential Signal-to-Noise Ratio of about 100 i.e. 20 dB, and with a ROI-to-background Signal-to-Noise Ratio of 43 dB. Observation of figure 4(d) highlights the need for establishing an adjacency relationship map between nodes.

3. Method

3.1. Node localization and neighbour relationship

Developing an automated solution for locating the apparent position of nodes in images cannot disregard determining the adjacency graph between them. Note that, if two nodes had to be erroneously established as neighbours, that is without a branch connecting them, this labelling error would propagate, flawing any subsequent attempt to use the positions of the nodes. This is true, even if their positions had been accurately determined. Previous works [2, 3] do not argument on this issue, in our opinion because they consider MRI systems with a limited geometric and through-plane distortion.

The flow diagram for our method is shown in Figure 5. It starts from the approximate positioning and operator-aided labelling of a node $\mathbf{p}_0$ in the set of acquired images. The labelling (row, column, slice) can be obtained by counting the number of grids encountered in each coordinate direction. The approximate position of the first point is used as a seed to determine an accurate estimate, along with unit vectors $(\mathbf{v}_x, \mathbf{v}_y, \mathbf{v}_z)$ for the branches departing from it. Estimation of the unit vectors for a cross (subsection 3.2) can be carried out before estimating the position of its node (subsections 3.3, 3.4).

The refined position and its related unit vectors are stored into a list L of nodes to be visited, while the refined position is output to a 3D structure C, filled with fiducial point apparent position estimates. This structure contains at address (row, column, slice) the estimate of the apparent position of the corresponding node in images and will enable fiducial point position estimation and processing methods like the one we described in [1]. Note that the address (row, column, slice) of a refined node position estimate in C defines the adjacency relationship between nodes.

The proposed method consists in extracting from L the position and unit vectors of the node $\mathbf{p}$ having the smallest norm and exploiting its unit vectors to determine the (up to six) approximate positions of its adjacent nodes (subsection 3.5) temporarily stored in a neighbour list NL. Each candidate neighbour is refined and its unit vectors are determined.
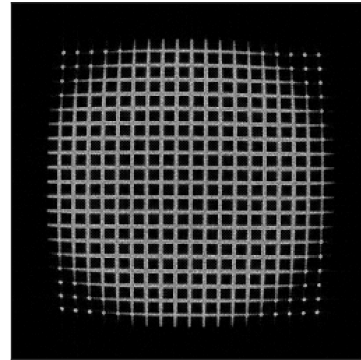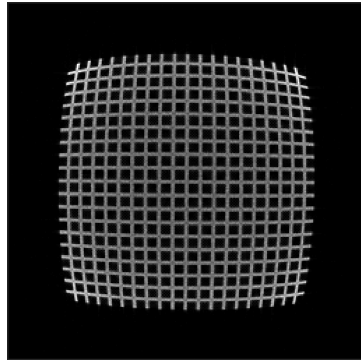
8

(a) Simulated image (XY) at isocentre

(b) Simulated image (XY) at 60 mm from isocentre
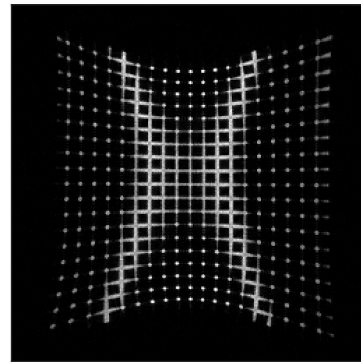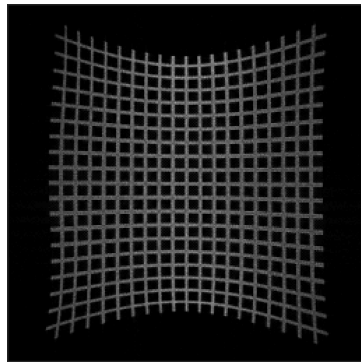
(c) Simulated image (ZX) at isocentre

(d) Simulated image (ZX) at 60 mm from isocentre

Figure 4: Geometric distortion in 3D Gradient Echo simulated images of our 3D grid phantom. The static field B_0 is nominally oriented along the Z axis, between the C-shaped permanent magnet poles.

9

For each refined neighbour, we test if C already includes a node that is close to it (less than one voxel). In this case the candidate neighbour is discarded because it has already been visited. Otherwise, we check it for satisfaction of a geometric distortion smoothness test. The criterion we devised is based on the assumption that the deformation undergone by the phantom is continuous. Specifically, we require that the angles described by a sequence of contiguous branches in the same direction do not vary more than $15°$. We chose this value considering that the angle we expect to see for a not directly-connected node in absence of distortion is at least $45°$. If this test is not passed, the refined node position is discarded. Otherwise, the refined neighbour node position is added to C and the node is added to L together with its unit vectors. The algorithm stops when the list L is empty.

3.2. Branch directions estimation

We decided to factor the problem of estimating the apparent position of a node in images in two steps: direction estimation with unknown positions, followed by direction-aided position estimation. The main reason for not using a 3D Hough transform [10, 11] is that the parameter space has four dimensions and our features are not point clouds in space, but continuously varying image intensities, so that direct application of the 3D Hough transform would require definition of thresholds and/or resampling.

Starting from the approximate location of a node, the first step to obtain its accurate position consists in identifying the unit vectors for the branches in its neighbourhood. These unit vectors allow us to build an ad-hoc, adaptive, cross prototype that makes node positioning more reliable and robust to geometric distortion.

We denote with $f(i, j, k)$ the intensity of the voxel at address (i, j, k) in the acquired volume, with $0 \leq i < N$, $0 \leq j < N$, $0 \leq k < N$. We will assume, for the sake of simplicity, that voxels are cubic with size $s = FOV/N$. Let

$$I_{0,r} = \{(i, j, k) : i_0 - r \leq i \leq i_0 + r, j_0 - r \leq j \leq j_0 + r, k_0 - r \leq k \leq k_0 + r\}$$

a cubic r-neighbourhood of the voxel (i_0, j_0, k_0), and

$$f_{I_{0,r}} = \begin{cases} f(i - i_0, j - j_0, k - k_0) & (i, j, k) \in I_{0,r} \\ 0 & \text{otherwise} \end{cases} \tag{2}$$

the restriction of $f(i, j, k)$ to $I_{0,r}$ referred to its centre.

It is well-known that the self-covariance function has local maxima for arguments equal to the offsets at which the signal is self-similar. For this reason, we use it to highlight the directions of the branches present in the neighbourhood of a cross, $f_{I_{0,r}}$. The diameter $D = 2r + 1$ of $I_{0,r}$ must be chosen according to phantom geometry and voxel size, ensuring the presence of at least one branch for each coordinate direction, i.e. we choose $r = \lceil (h/2 + \phi)/s \rceil = 8$ voxel for the phantom geometry of Fig. 4.
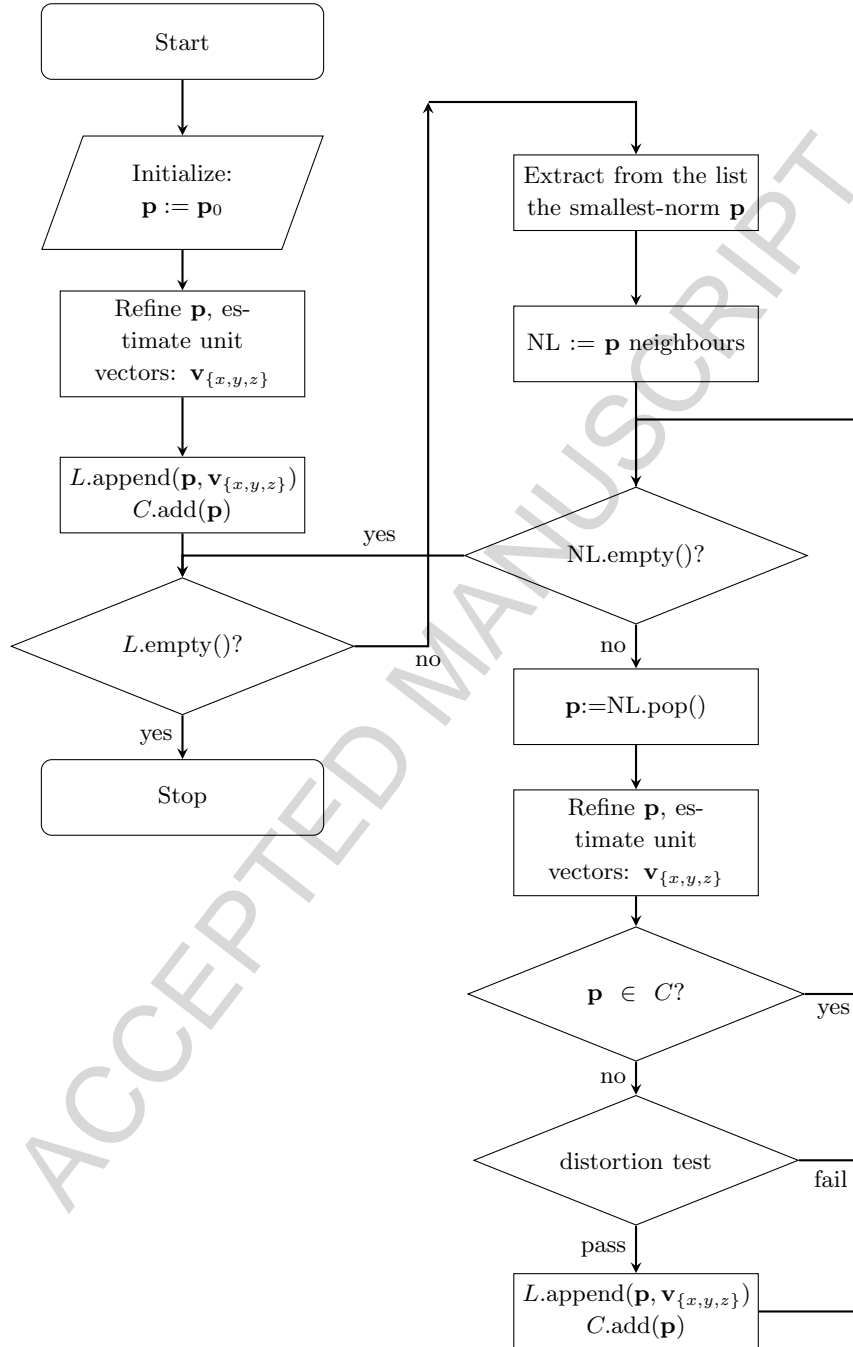
10

Figure 5: Flow-Chart for the node position and adjacency relationship assessment algorithm.
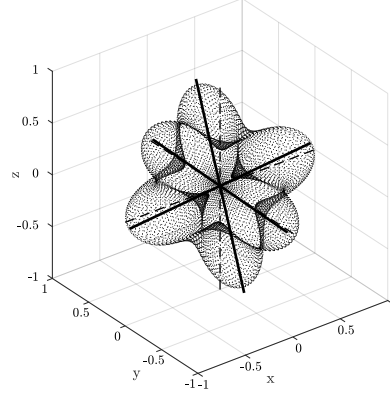
Figure 6: Scatterplot of the unit vectors used to search branch directions, scaled proportionally to the inner product between $C(n, m, l)$ and the bar prototypes. Dashed lines are the coordinate axes. Thick lines denote the estimated directions

Denoting with $\overline{f_{I_{0,r}}}$ the average intensity of $f_{I_{0,r}}$, its self-covariance will be given by

$$C(n, m, l) = \sum_{i,j,k} (f_{I_{0,r}}(i, j, k) - \overline{f_{I_{0,r}}})(f_{I_{0,r}}(i+n, j+m, k+l) - \overline{f_{I_{0,r}}}). \quad (3)$$

In order to extract the directions of the branches from $C(n, m, l)$, we constructed a set of segment-prototypes with thickness ϕ starting from the centre of the neighbourhood and uniformly oriented in space [11]. The prototypes have been shaped in order to limit the effect of the large maximum shown by the self-covariance around the origin. The number V of prototypes to consider must be high enough to approximate continuity, but not too high, to avoid undistinguishable prototypes and waste of computing resources. We found a good number of directions is $V = 10242$ (obtained by refining the mesh of an icosahedron). The search for the branch unit-vectors found in the neighbourhood of a cross is carried out by computation of all inner products between these segment prototypes and the self-covariance of the neighbourhood of the cross. Figure 6 shows an example scatterplot of the directions used for the unit-vectors search, scaled to amplitudes proportional to the inner products between the bar prototypes and the self-covariance of a representative cross-neighbourhood. The dashed lines show the coordinate axes, while the thick lines show the estimated directions of the unit-vectors useful to build the cross prototype.

3.3. Cross-prototype

Under the hypothesis of availability of a cross-prototype, its node can be located by searching for cross-covariance maxima. Previous works [3, 4] choose

12

spheres as recognizable structures in images, and obtain the fiducial point locations by means of cross-correlation with a sphere prototype whose geometry is argued to not be significantly affected by geometric distortion.

In our case, the local features of the phantom are strongly influenced by geometric distortion and it is therefore not possible to use the same cross-prototype for all nodes, but it is instead necessary to build an ad-hoc cross-prototype for each node, based on the directions of the branches that depart from it. In particular, given three unit-vectors $(\mathbf{v}_x, \mathbf{v}_y, \mathbf{v}_z)$ and the branch thickness, we model the 3D image intensity in the neighbourhood of a node centred in the origin as follows:

$$p_{\mathbf{v}_x \mathbf{v}_y \mathbf{v}_z}(x, y, z) = 1 - \prod_{\mathbf{v}=\mathbf{v}_x, \mathbf{v}_y, \mathbf{v}_z} [1 - \mathrm{RC}(\alpha, \phi, \delta(x, y, z, \mathbf{v}))] \tag{4}$$

where $\delta(x, y, z, \mathbf{v}) = ||(x, y, z) - \langle(x, y, z), \mathbf{v}\rangle\mathbf{v}||$ is the distance of the point from the line passing through the origin, and $\mathrm{RC}(\alpha, \phi, \delta)$ denotes a raised-cosine function:

$$\mathrm{RC}(\alpha, \phi, \delta) = \begin{cases} 1 & \delta \leq \frac{\phi - \alpha}{2} \\ \cos^2\left(\frac{\pi}{2\alpha}\left(\delta - \frac{\phi - \alpha}{2}\right)\right) & \frac{\phi - \alpha}{2} < \delta \leq \frac{\phi + \alpha}{2} \\ 0 & \delta > \frac{\phi + \alpha}{2} \end{cases}$$

The parameter α denotes the width of the transition interval from maximum intensity to no signal and we set it equal to the size s of a voxel. We chose the raised cosine as a good finite-support profile with good spectral properties. The rasterization of the neighbourhood of a node is obtained by sampling $p_{\mathbf{v}_x \mathbf{v}_y \mathbf{v}_z}$ in (is, js, ks).

The outlined procedure yields a cross prototype centred in the origin. The cross prototype $P_{\mathbf{v}_x, \mathbf{v}_y, \mathbf{v}_z}(i, j, k, \epsilon)$ of a node centred in $\epsilon = (\epsilon_x, \epsilon_y, \epsilon_z)$ will be obtained by sampling:

$$P_{\mathbf{v}_x, \mathbf{v}_y, \mathbf{v}_z}(i, j, k, \epsilon) = p_{\mathbf{v}_x \mathbf{v}_y \mathbf{v}_z}(is - \epsilon_x, js - \epsilon_y, ks - \epsilon_z).$$

3.4. Accurate node-position estimation

Once the ad-hoc cross-prototype $P_{\mathbf{v}_x, \mathbf{v}_y, \mathbf{v}_z}$ is available, the node can be located by computing its cross-correlation with $f_{I_{0,r}}$ as follows:

$$\Gamma(n, m, l, \epsilon) = \sum_{i,j,k} P_{\mathbf{v}_x, \mathbf{v}_y, \mathbf{v}_z}(i, j, k, \epsilon) f_{I_{0,r}}(i + n, j + m, k + l). \tag{5}$$

This function has a maximum at the offset (m_0, n_0, l_0) needed to move from the centre (i_0, j_0, k_0) of the neighbourhood to the estimate position $(i'_0, j'_0, k'_0) = (i_0 + m_0, j_0 + n_0, k_0 + l_0)$ of the node. Computation of $\Gamma(n, m, l, \epsilon)$ can be performed efficiently through FFT. In any case, this method has a voxel-size resolution and therefore results in a coarse estimate.
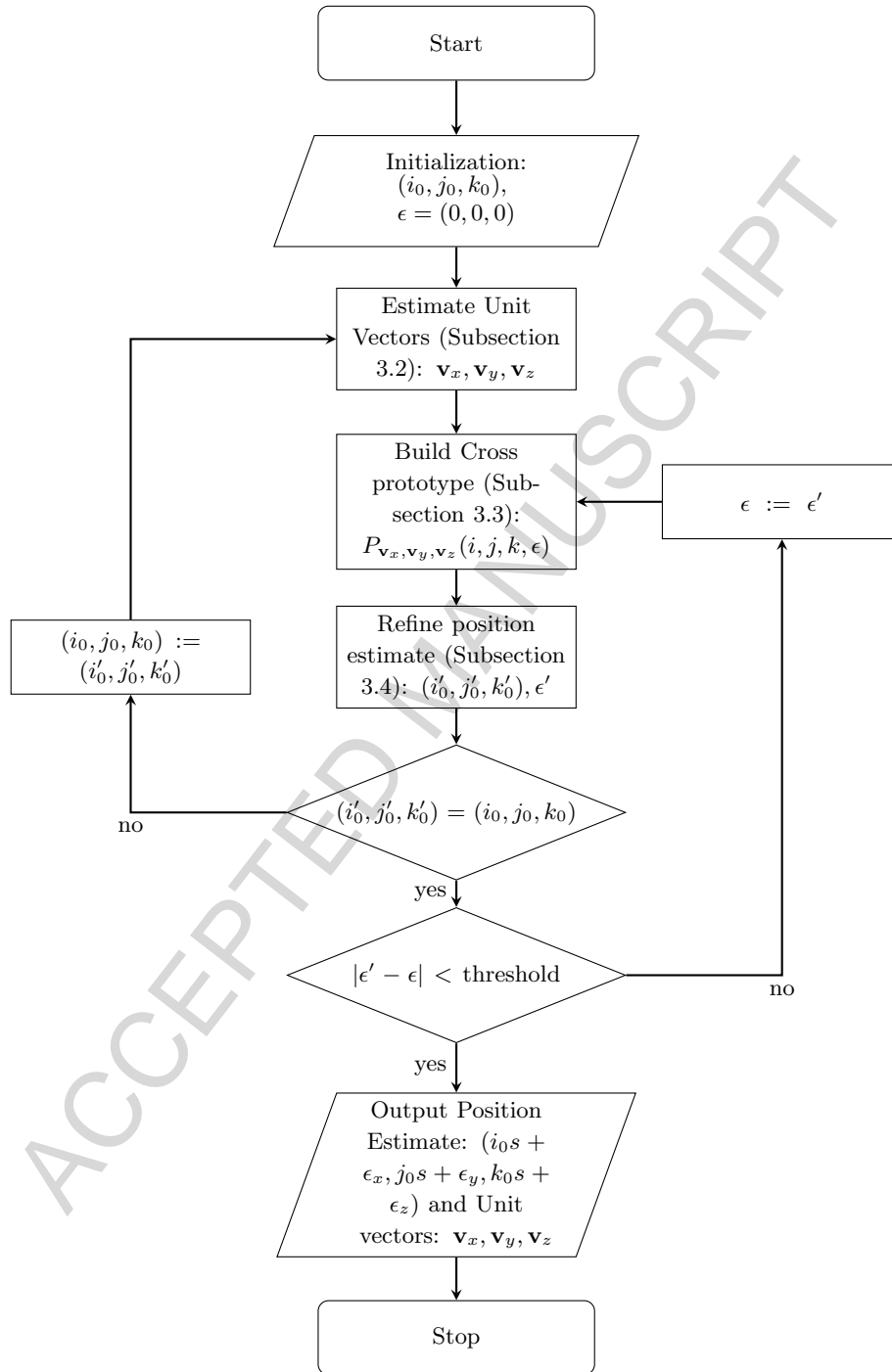
13

Start

Initialization:
(i_0, j_0, k_0),
$\epsilon = (0, 0, 0)$

Estimate Unit Vectors (Subsection 3.2): $\mathbf{v}_x, \mathbf{v}_y, \mathbf{v}_z$

Build Cross prototype (Subsection 3.3): $P_{\mathbf{v}_x, \mathbf{v}_y, \mathbf{v}_z}(i, j, k, \epsilon)$

$\epsilon := \epsilon'$

$(i_0, j_0, k_0) := (i_0', j_0', k_0')$

Refine position estimate (Subsection 3.4): $(i_0', j_0', k_0'), \epsilon'$

$(i_0', j_0', k_0') = (i_0, j_0, k_0)$

no

yes

$|\epsilon' - \epsilon| < \text{threshold}$

no

yes

Output Position Estimate: $(i_0 s + \epsilon_x, j_0 s + \epsilon_y, k_0 s + \epsilon_z)$ and Unit vectors: $\mathbf{v}_x, \mathbf{v}_y, \mathbf{v}_z$

Stop

Figure 7: Flow-Chart for the iterative node-location estimation algorithm.
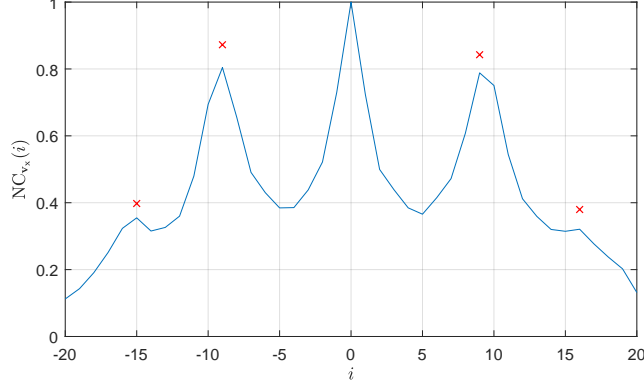
14

Figure 8: Normalized cross correlation sampled along unit vector $\mathbf{v}_x$ (example). Red marks denote the maxima found in a 27-voxel volume around each of the local maxima.

In order to obtain sub-voxel positioning of nodes, we compute the following fine adjustments:

$$\epsilon_x' = \epsilon_x + \frac{s}{2} \frac{\Gamma(m_0 - 1, n_0, l_0, \epsilon) - \Gamma(m_0 + 1, n_0, l_0, \epsilon)}{\Gamma(m_0 - 1, n_0, l_0, \epsilon) - 2\Gamma(m_0, n_0, l_0, \epsilon) + \Gamma(m_0 + 1, n_0, l_0, \epsilon)} \qquad (6)$$

$$\epsilon_y' = \epsilon_y + \frac{s}{2} \frac{\Gamma(m_0, n_0 - 1, l_0, \epsilon) - \Gamma(m_0, n_0 + 1, l_0, \epsilon)}{\Gamma(m_0, n_0 - 1, l_0, \epsilon) - 2\Gamma(m_0, n_0, l_0, \epsilon) + \Gamma(m_0, n_0 + 1, l_0, \epsilon)} \qquad (7)$$

$$\epsilon_z' = \epsilon_z + \frac{s}{2} \frac{\Gamma(m_0, n_0, l_0 - 1, \epsilon) - \Gamma(m_0, n_0, l_0 + 1, \epsilon)}{\Gamma(m_0, n_0, l_0 - 1, \epsilon) - 2\Gamma(m_0, n_0, l_0, \epsilon) + \Gamma(m_0, n_0, l_0 + 1, \epsilon)} \qquad (8)$$

These refinements are based on a parabolic interpolation of $\Gamma(m, n, l, \epsilon)$ around its maximum at (m_0, n_0, l_0). The fine estimate for the position of a node will be $(i_0' s + \epsilon_x', j_0' s + \epsilon_y', k_0' s + \epsilon_z')$.

We argue that, if the estimated position were to coincide with the true one, repeating the procedure starting from a neighbourhood centred in (i_0', j_0', k_0') and cross correlating with a cross-prototype centred in $(\epsilon_x', \epsilon_y', \epsilon_z')$ we would obtain a maximum in $(m_0', n_0', l_0') = (0, 0, 0)$ and the same set of adjustments $(\epsilon_x', \epsilon_y', \epsilon_z')$. On the basis of this considerations, we implemented an iterative algorithm, whose flow chart is shown in Figure 7, to obtain accurate sub-voxel estimates for the apparent positions of a node, together with its associated unit-vectors $(\mathbf{v}_x, \mathbf{v}_y, \mathbf{v}_z)$. The iteration stopping threshold can be set to an arbitrarily small positive value, and we used $1\mu m$. Rarely, in our experiments below 1% of cases, the algorithm will not converge under this threshold, oscillating between a number of points in space. In this case our algorithm outputs as estimate the average location from a period of oscillation.

3.5. Iterative construction of the adjacency relationship between nodes

Adoption of the methods described in sections 3.2-3.4 allows to accurately locate a node and determine the apparent directions of the branches originating

15

from it, starting from a non-necessarily centred neighbourhood of the node. In order to complete a recursion as described in section 3.1, it is necessary to determine the approximate positions of the adjacent nodes, that have to be correctly labelled (row, column, slice) and inserted into the list NL of points to be visited.

To this end, we define the normalized cross-correlation function between the restrictions of $f(i, j, k)$ to two neighbourhoods $I_{0,r}$ and $I_{0,q}$ with $q > r$, as

$$\mathrm{NC}(n, m, l) = \frac{\sum\limits_{i,j,k=-r}^{r} f_{I_{0,r}}(i, j, k) f_{I_{0,q}}(i+n, j+m, k+l)}{\sqrt{\sum\limits_{i,j,k=-r}^{r} f_{I_{0,r}}^2(i, j, k) \sum\limits_{i,j,k=-r}^{r} f_{I_{0,q}}^2(i+n, j+m, k+l)}} \tag{9}$$

where the offsets (n, m, l) must have module not greater than $q - r$ in order to avoid edge effects, and the denominator is a normalization factor obtained interpreting the numerator as an inner product between sequences having support D^3. The normalized cross correlation function has significant maxima in correspondence of nodes (adjacent or not) present in the neighbourhood $I_{0,q}$.

Since we are interested in the adjacent nodes only, the selection of the corresponding maxima can be performed by looking for them along the directions identified by the node's unit vectors. E.g. in order to search for the maxima along the direction identified by the unit vector $\mathbf{v}_x = (v_{x1}, v_{x2}, v_{x3})$, we define $j_{\mathbf{v}_x}(i) = \lfloor v_{x2}i/v_{x1} \rfloor$, $dj_{\mathbf{v}_x}(i) = v_{x2}i/v_{x1} - j_{\mathbf{v}_x}(i)$, $k_{\mathbf{v}_x}(i) = \lfloor v_{x3}i/v_{x1} \rfloor$, $dk_{\mathbf{v}_x}(i) = v_{x3}i/v_{x1} - k_{\mathbf{v}_x}(i)$ and use bilinear interpolation to sample $\mathrm{NC}(n, m, l)$ as follows:

$$\begin{aligned}
\mathrm{NC}_{\mathbf{v}_x}(i) = &(1 - dj_{\mathbf{v}_x}(i))(1 - dk_{\mathbf{v}_x}(i))\mathrm{NC}(i, j_{\mathbf{v}_x}(i), k_{\mathbf{v}_x}(i)) \\
&+ dj_{\mathbf{v}_x}(i)(1 - dk_{\mathbf{v}_x}(i))\mathrm{NC}(i, j_{\mathbf{v}_x}(i) + 1, k_{\mathbf{v}_x}(i)) \\
&+ (1 - dj_{\mathbf{v}_x}(i))dk_{\mathbf{v}_x}(i)\mathrm{NC}(i, j_{\mathbf{v}_x}(i), k_{\mathbf{v}_x}(i) + 1) \\
&+ dj_{\mathbf{v}_x}(i)dk_{\mathbf{v}_x}(i)\mathrm{NC}(i, j_{\mathbf{v}_x}(i) + 1, k_{\mathbf{v}_x}(i) + 1)
\end{aligned} \tag{10}$$

Figure 8 shows an example of a sampled NC profile. For each local maximum, we further refine the search in a 27-voxel cubic volume around it, and the resulting maxima are shown as red marks. Only the highest local maximum is added to the list NL of neighbours to visit.

4. Results

4.1. Impact of Signal-to-Noise Ratios and Phantom geometry

The Spherical Harmonics expansions we used have been obtained by a magnetometer having a radius of 125 mm. We simulated several possible geometries for the phantom described in section 2, while keeping the same volume for the cube enclosing all nodes. Table 1 shows the parameters we adopted in terms of
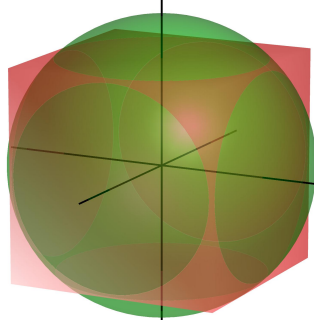
16

Figure 9: Rendering of the cube (with a edge length of 180 mm) containing all fiducial points with respect to the homogeneity sphere (radius 125 mm).

h: distance between nodes	nodes per dimension	number of nodes	overall phantom edge length	edge length of the cube enclosing nodes
10 mm	19	6859	190 mm	180 mm
18 mm	11	1331	198 mm	180 mm
22.5 mm	9	729	200.5 mm	180 mm

Table 1: Simulated phantom geometries. The volume of the cube enclosing all nodes is constant.

distance between adjacent nodes h and number of nodes per dimension, while figure 9 shows the relationship between the phantom and the homogeneity sphere. We used a order $l_{max} = 7$ Spherical Harmonics expansion. It is worthwhile observing that some nodes of the simulated phantom will lay outside of the homogeneity sphere, so that the adopted Spherical Harmonics expansion will not represent the reference MRI system fields, but can nonetheless be used to evaluate the performance of our method.

The first performance figures we report are intended to show the impact of the differential Signal-to-Noise Ratio on localization accuracy. Table 2 shows how the mean displacement error $E[d]$ between the localized node and its theoretical counterpart decreases from 0.1 to 0.04 mm when increasing the differential SNR from 3.2 to 30.2 dB. The theoretical distorted positions can be computed for example as shown in [12, 13], and will be already available in any MRI system featuring correction of geometric distortion. We added, in the last column of all tables, the displacement error 0.99 quantile, i.e. the displacement error only 1% the located points are above. Note that all of the fiducial points have been successfully located.

In order to evaluate the impact of the ROI-to-background SNR on the robustness and accuracy of fiducial points localization, we report in Table 3 the performance of the proposed method with Signal-to-Noise Ratios down to 3 dB i.e. with a standard deviation of background voxels equal to half of the average intensity within the ROI. At this noise level, a human observer finds difficult to discern the features of the phantom from the background. The proposed

17

Proj.	SNR_{diff}	missing nodes	$\text{E}[d]$	σ_d	0.99 quantile
XY	3.2 dB	0	0.1003 mm	0.0447 mm	0.2308 mm
XY	7.2 dB	0	0.0687 mm	0.0308 mm	0.1561 mm
XY	10.2 dB	0	0.0576 mm	0.0260 mm	0.1384 mm
XY	13.2 dB	0	0.0486 mm	0.0212 mm	0.1145 mm
XY	17.2 dB	0	0.0433 mm	0.0196 mm	0.1071 mm
XY	20.2 dB	0	0.0415 mm	0.0185 mm	0.1012 mm
XY	23.2 dB	0	0.0401 mm	0.0181 mm	0.1016 mm
XY	27.2 dB	0	0.0400 mm	0.0181 mm	0.09502 mm
XY	30.2 dB	0	0.0394 mm	0.0180 mm	0.09740 mm

Table 2: Localization performance with increasing differential Signal-to-Noise Ratios (simulated point density), for the same phantom geometry ($h = 18$ mm, $\phi = 3$ mm).

Proj.	SNR	missing nodes	$\text{E}[d]$	σ_d	0.99 quantile
XY	∞	0	0.0433 mm	0.0196 mm	0.1071 mm
XY	40 dB	0	0.0433 mm	0.0197 mm	0.1050 mm
XY	30 dB	0	0.0438 mm	0.0197 mm	0.1073 mm
XY	20 dB	0	0.0471 mm	0.0211 mm	0.1103 mm
XY	10 dB	0	0.0736 mm	0.0331 mm	0.1758 mm
XY	3 dB	1	0.1527 mm	0.1269 mm	0.4141 mm

Table 3: Localization performance with increasing (AWGN) Signal-to-Noise Ratios, for the same phantom geometry ($h = 18$ mm, $\phi = 3$ mm, $\text{SNR}_{\text{diff}} = 17.2$ dB).

method is very robust to noise, since the Normalized Cross Covariance with a large prototype such as the *adaptive* one we devised acts as a filter with respect to noise. One of the fiducial points was missing at the lowest SNR case, and we found that the localization algorithm failed to identify the unit vectors needed to build the cross prototype.

As a trade-off between simulation speed and localization performance[4], we chose to run the rest of simulations with an SNR_{diff} of 20.2 dB, i.e. a random point density of 100 points/mm^3 and a ROI-to-background SNR or 100 (i.e. 20 dB). Figures 4 have been obtained with this spatial point density. Note that a MRI system passing the ACR QA Accreditation test will have higher Signal-to-Noise Ratios on images of a phantom.

Table 4 reports the localization performance for phantoms having a feature thickness $\phi = 3$ mm, with the three geometries of table 1 and the three canonical projections (Coronal, Sagittal, Axial). The average displacement error is always lower than 0.07 mm. Inspection of the table shows that the $h = 18$ mm geometry has slightly better performance than $h = 10$ mm and $h = 22.5$ mm. In our opinion, this is due to the fact that the prototype used for $h = 10$ mm is smaller and has a lower resilience to noise, while the $h = 22.5$ mm prototype resulted relatively too large in order to fit the curvature of the distorted images.

---

[4]Our simulation software employs the Non-Uniform FFT algorithm [8, 9] to accelerate the computation of (1)

Proj.	h	ϕ	missing nodes	E[d]	σ_d	0.99 quantile
XY	10 mm	3 mm	0	0.0560 mm	0.0252 mm	0.1291 mm
XZ	10 mm	3 mm	1	0.0571 mm	0.0257 mm	0.1333 mm
YZ	10 mm	3 mm	1	0.0579 mm	0.0265 mm	0.1367 mm
XY	18 mm	3 mm	0	0.0515 mm	0.0226 mm	0.1212 mm
XZ	18 mm	3 mm	0	0.0536 mm	0.0289 mm	0.1561 mm
YZ	18 mm	3 mm	0	0.0540 mm	0.0301 mm	0.1700 mm
XY	22.5 mm	3 mm	0	0.0578 mm	0.0267 mm	0.1334 mm
XZ	22.5 mm	3 mm	0	0.0631 mm	0.0407 mm	0.2473 mm
YZ	22.5 mm	3 mm	0	0.0644 mm	0.0419 mm	0.2537 mm

Table 4: Localization performance for the three ortogonal projections ($\text{SNR}_{\text{diff}} = 20.2\,\text{dB}$, ROI-to-background SNR=20 dB).

Proj.	h	ϕ	missing nodes	E[d]	σ_d	0.99 quantile
XY	18 mm	3 mm	0	0.0458 mm	0.0178 mm	0.0952 mm
XZ	18 mm	3 mm	0	0.0452 mm	0.0175 mm	0.0889 mm
YZ	18 mm	3 mm	0	0.0451 mm	0.0179 mm	0.0900 mm

Table 5: Localization performance with ideal fields (constant B_0, linear gradients) and every coordinate projection, for a same phantom geometry.

Note that XY-plane (coronal) images exhibit better performance than XZ-plane or YZ-plane (sagittal, axial) ones. This may be justified by recalling that our SHC sets are from an open-bore 0.3 T C-shaped permanent magnet system having a main field oriented along Z, with an inevitable more significant non-linearity for the X- and Y-axis gradient fields resulting in a higher geometric distortion (also due to the main field inhomogeneity) in sagittal and axial projections. In order to verify this conjecture we simulated three sets with ideal fields (obtained by stopping the Spherical Harmonics Expansion to $l_{max} = 1$), whose performance is reported in Table 5. This table provides a effective lower bound on localization error for $\text{SNR}_{\text{diff}} = 20.2\,\text{dB}$ and a ROI-to-background SNR of 20 dB, and shows that there is no difference in localization performance between the projections with ideal fields.

Last, Table 6 shows the localization performance for different values of branch thickness ϕ, for a node distance $h = 18\,\text{mm}$. We observe that $\phi = 3\,\text{mm}$

Proj.	ϕ	missing nodes	E[d]	σ_d	0.99 quantile
XY	2 mm	0	0.0684 mm	0.0281 mm	0.1393 mm
XY	3 mm	0	0.0515 mm	0.0226 mm	0.1212 mm
XY	4 mm	0	0.0560 mm	0.0260 mm	0.1373 mm
XY	5 mm	1	0.0611 mm	0.0319 mm	0.1651 mm
XY	6 mm	11	0.0737 mm	0.0856 mm	0.2330 mm
XY	7 mm	44	0.1104 mm	0.1083 mm	0.5838 mm

Table 6: Localization performance with increasing cross thickness ϕ and every coordinate projection, for phantoms with $h = 18\,\text{mm}$, $\text{SNR}_{\text{diff}} = 20.2\,\text{dB}$, ROI-to-background SNR=20 dB.
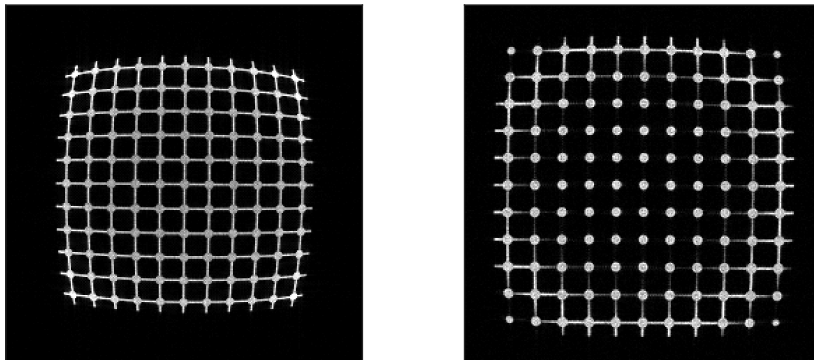
(a) Simulated image (XY) at isocentre

(b) Simulated image (XY) at 71 mm from isocentre

Figure 10: Simulated images for a Sphere-based phantom similar to the one reported in [3].

exhibits the best performance. Thinner features, that are expected to provide better accuracy, seem to suffer from noise. Thick ones, conversely, result relatively more difficult to localize (the mean displacement error for $\phi = 5$ mm is still lower than 0.07 mm), but could be preferred in order to manufacture a phantom, since they will suffer less from air bubbles. The number of missing nodes for phantoms with thick features increases abruptly. We inspected the set of missing nodes and found that, due to the geometrical distortion, the fit between our proposed cross prototype and the distorted image is not good. In fact, our proposed prototype features adaptive unit vectors directions, but does not adapt its feature thickness to the geometric distortion.

4.2. Comparison to a sphere-based method

In order to validate our proposed method, we report localization results for the sphere-based method proposed by Huang *et al* [3]. Their method was created to assess the accuracy of geometric correction on a 3 T MRI system, so the residual geometric distortion is limited. Their phantom is made of a 3D lattice of spheres having a 7 mm diameter connected by thin tubes (we estimated 2 mm diameter from the paper). The structure is filled with an MR-visible solution, and the localization is based on searching maxima of an *oversampled* normalized cross correlation to a set of (full or partially full) sphere prototypes.

Since our purpose is localization of fiducial points in raw, uncorrected images, we expect any method based on a not-adaptive prototype to perform poorly. In order to evaluate the method, we modified our simulator to feature spheres instead of crosses, and thin branches between spheres. Two simulated images are shown in Figure 10.

20

Proj.	γ_{thr}	cluster averaging	missing nodes	E[d]	σ_d	0.99 quantile
XY	0.7	Y	0	0.1981 mm	0.1336 mm	0.8168 mm
XY	0.7	N	0	0.1725 mm	0.0734 mm	0.3905 mm
XY	0.8	Y	9	0.1950 mm	0.1243 mm	0.7520 mm
XY	0.8	N	9	0.1785 mm	0.1040 mm	0.4564 mm
XY	0.9	Y	398	0.1650 mm	0.05278 mm	0.2746 mm
XY	0.9	N	398	0.1643 mm	0.05228 mm	0.2744 mm

Table 7: Localization performance for phantoms with $h = 18$ mm, $\mathrm{SNR}_{\mathrm{diff}} = 20.2$ dB, ROI-to-background SNR=20 dB. We adopted an oversampling factor of 3, as reported in [3]

Proj.	OSF	cluster averaging	missing nodes	E[d]	σ_d	0.99 quantile
XY	1	Y	0	0.4841 mm	0.1424 mm	0.7504 mm
XY	1	N	0	0.4835 mm	0.1419 mm	0.7490 mm
XY	2	Y	0	0.2442 mm	0.07390 mm	0.3921 mm
XY	2	N	0	0.2437 mm	0.07348 mm	0.3908 mm
XY	3	Y	0	0.1649 mm	0.05206 mm	0.2735 mm
XY	3	N	0	0.1649 mm	0.05206 mm	0.2735 mm

Table 8: Localization performance for sphere-featuring phantoms with $h = 18$ mm, $\mathrm{SNR}_{\mathrm{diff}} = 20.2$ dB, ROI-to-background SNR=20 dB. We used ideal fields (obtained with an Spherical Harmonics expansion having $l_{\max} = 1$)

In [3], the position of a fiducial point is estimated as the position of a Normalized Cross Correlation local maximum whose value is above a given threshold γ_{thr}. When a set of connected voxels has a NCC value above the threshold, the authors estimate the fiducial point location as the mean position of the connected set. We refer to this option as *cluster averaging* rather than taking as estimate the position of the maximum within the cluster.

Table 7 reports the localization results for different choices of Normalized Cross Correlation threshold γ_{thr} and cluster averaging choice. Inspection of the table shows that higher thresholds, while yielding more accurate estimates, lead to massive loss of fiducial points. This is readily explained since the fixed-diameter sphere prototype does not fit well the image when the distortion is substantial. We found that, with our simulated images, choosing the local maximum within a cluster performs better than cluster averaging. A comparison of Tables 6 and 7 shows that our method outperforms the one reported in [3], by a factor of about three, depending on phantom parameters. This has in our opinion a two-fold justification. First, the method reported in [3] was not designed to work on distorted images but on geometrically corrected ones. Second, we believe that the accuracy of that method is limited by the resolution of images.

In fact, we simulated their phantom with ideal fields, and values of interpolating ratio (denoted by OSF) between 1 (no interpolation) and 3 (the value used in [3]), and repeated the localization. Results of this analysis are reported in table 8. Inspection of this table shows that, as expected, no nodes are missing, and the average location displacement results inversely proportional to the

21

interpolation factor. Indeed, the main improvement of our localization method with respect to the one described in [3] can be ascribed to the fine position estimation adjustment (6-8).

Last, it is worth noting that the fiducial point labelling issue is not addressed in [3], since they work on geometrical corrected images and the labelling is trivial in that case.

5. Conclusion

This paper deals with an automated method to determine the apparent positions of fiducial points in distorted images of an MRI phantom. In order to estimate the localization errors, we used simulated images obtained via an ad-hoc developed joint MRI phantom and sequence simulator.

To the best of our knowledge, the proposed method outperforms the state-of-the-art, obtains estimates having a very low average displacement from the theoretical distorted positions, and enables fiducial point-based post-processing methods that can be used for image registration, field map estimation, geometric distortion correction, or other applications where accurate localization of a voxel in space is needed, such as radio-therapy planning.

Further works will need to cover phantom manufacturing issues, in order to tackle the problem of air bubbles that our proposed structure may exhibit. Another possible extension is generalization of the geometrical distortion model for our fiducial point prototype, in order to improve the localization accuracy when the geometrical distortion is severe.

References

[1] R. Acquaviva, S. Mangione, G. Garbo, Image-based MRI Gradient Estimation, Magn. Reson. Imaging 2018 Jan 2. pii: S0730-725X(17)30304-1.

[2] D. Wang, D. M. Doddrell, G. Cowin, A novel phantom and method for comprehensive 3-dimensional measurement and correction of geometric distortion in magnetic resonance imaging, Magn. Reson. Imaging 22 (2004) 529–542.

[3] K. C. Huang, Y. Cao, U. Baharom, J. M. Balter, Phantom-based characterization of distortion on a magnetic resonance imaging simulator for radiation oncology, Phys Med Biol. 2016 Jan 21;61(2):774-90.

[4] P. T. Weavers, S. Tao, J. D. Trzasko, Y. Shu, E. J. Tryggestad, J. L. Gunter, K. P. McGee, D. V. Litwiller, K. Hwang, M. A. Bernstein, Image-based gradient non-linearity characterization to determine higher-order spherical harmonic coefficients for improved spatial position accuracy in magnetic resonance imaging, Magnetic Resonance Imaging 38 (2017) 54–62

[5] http://mathworld.wolfram.com/MonteCarloIntegration.html

[6] J. Michiels, H. Bosmans, P. Pelgrims, D. Vandermeulen, J. Gybels, G. Marchal, P. Suetens, On the problem of geometric distortion in magnetic resonance images for stereotactic neurosurgery, Magnetic resonance imaging 12 (5) (1994) 749–765.

[7] O. Dietrich, J. G. Raya, S. B. Reeder, M. F. Reiser, S. O. Schoenberg, Measurement of Signal-to-Noise Ratios in MR Images: Influence of Multichannel Coils, Parallel Imaging, and Reconstruction Filters, Journal of Magnetic Resonance Imaging 26, 2007, pp. 375–385

[8] L. Greengard, J.-Y. Lee, Accelerating the Nonuniform Fast Fourier Transform, SIAM Review 46, 443 (2004).

[9] J.-Y. Lee, L. Greengard, The type 3 nonuniform FFT and its applications, J. Comput. Phys. 206, 1 (2005).

[10] C. Dalitz, T. Schramke, M. Jeltsch, Iterative Hough Transform for Line Detection in 3D Point Clouds, Image Processing On Line, 7 (2017), pp. 184–196

[11] M. Jeltsch, C. Dalitz, R. Pohle-Frohlich, Hough parameter space regularisation for line detection in 3D, International Conference on Computer Vision Theory and Applications (VISAPP), 2016, pp. 345–352

[12] K. Sekihara, M. Kuroda, H. Kohno, Image restoration from non-uniform magnetic field influence for direct fourier nmr imaging, Phys. Med. Biol. 29 (1) (1984) 15–24.

[13] H. Chang, J. M. Fitzpatrick, A technique for accurate magnetic resonance imaging in the presence of field inhomogeneities, IEEE Trans Med Imaging 11 (3) (1992) 319–329.
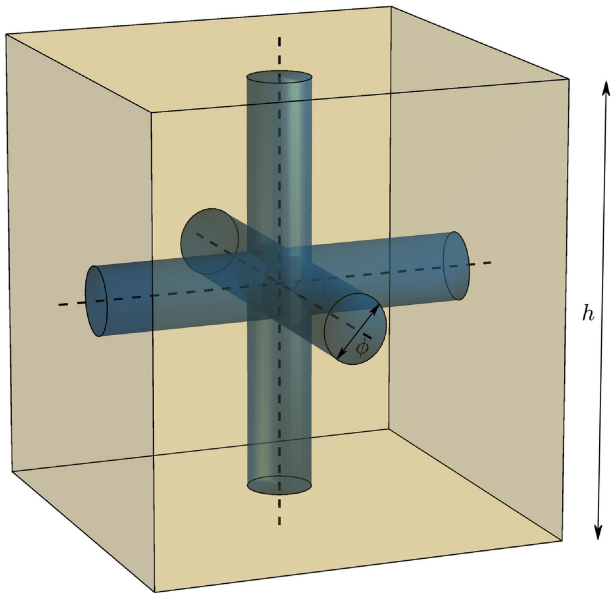
Figure 1
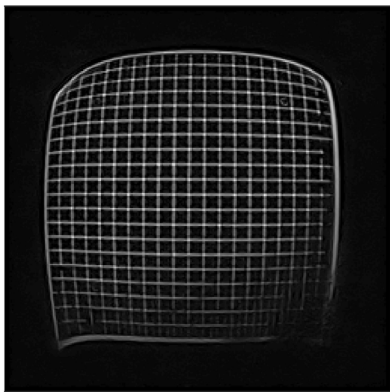
(a) Raw image at isocentre
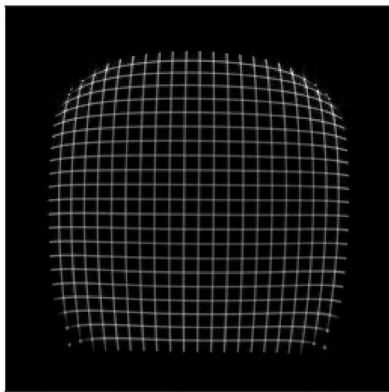
(b) Simulated image at isocentre
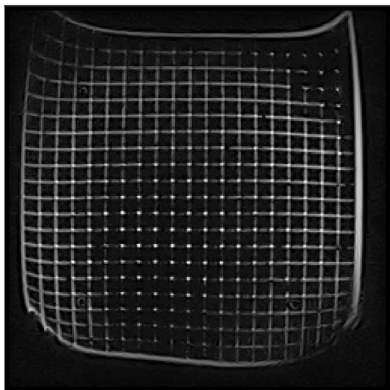
(c) Raw image at 60 mm from isocentre
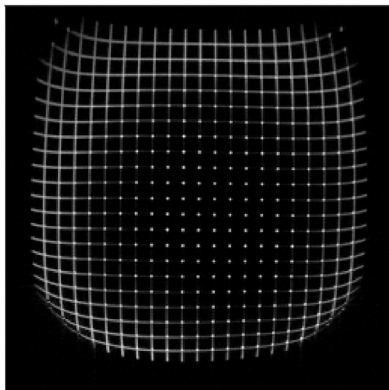
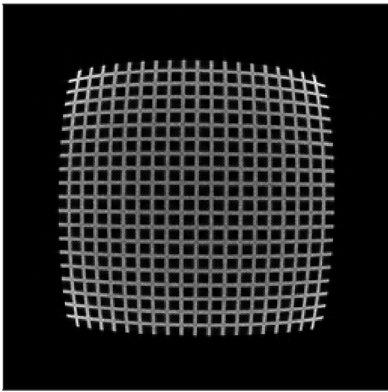(d) Simulated image at 60 mm from isocentre
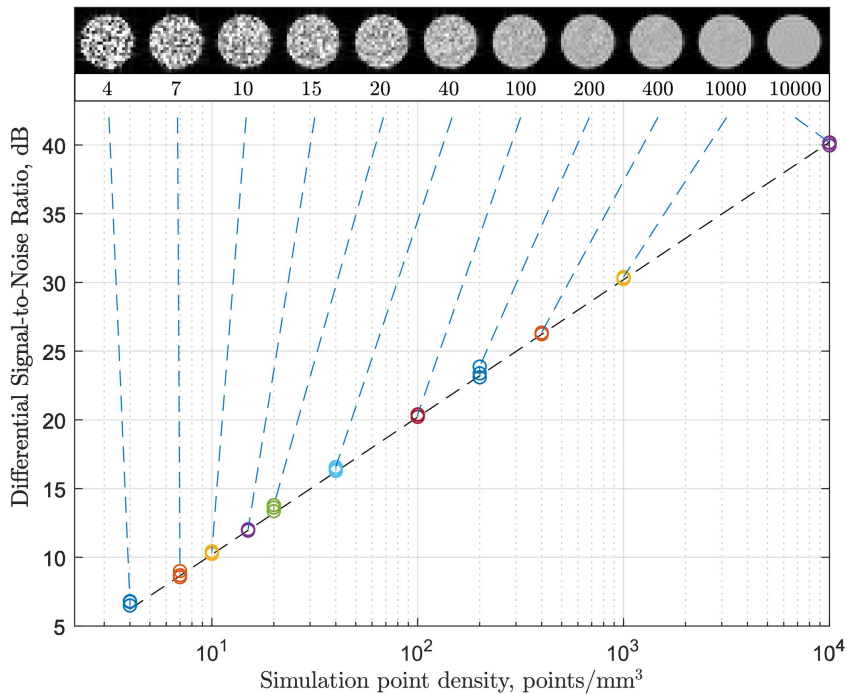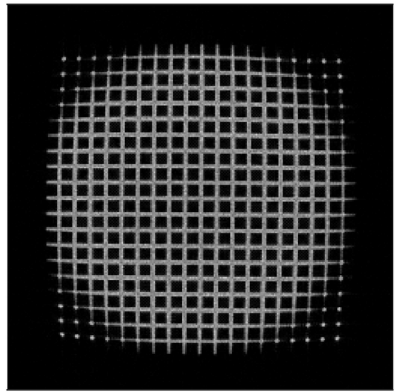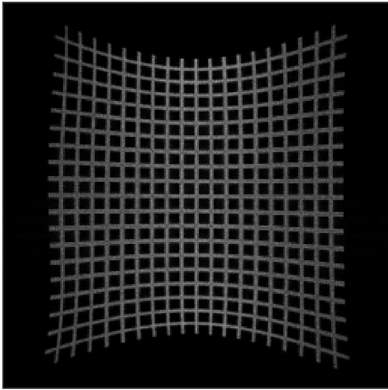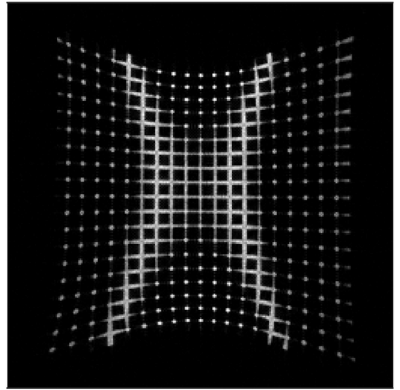
Figure 2

(a)
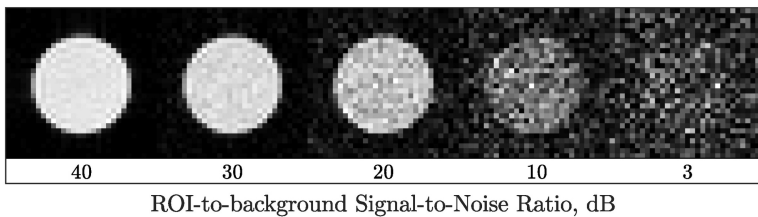
(b)

Figure 3

(a) Simulated image (XY) at isocentre

(b) Simulated image (XY) at 60 mm from isocentre

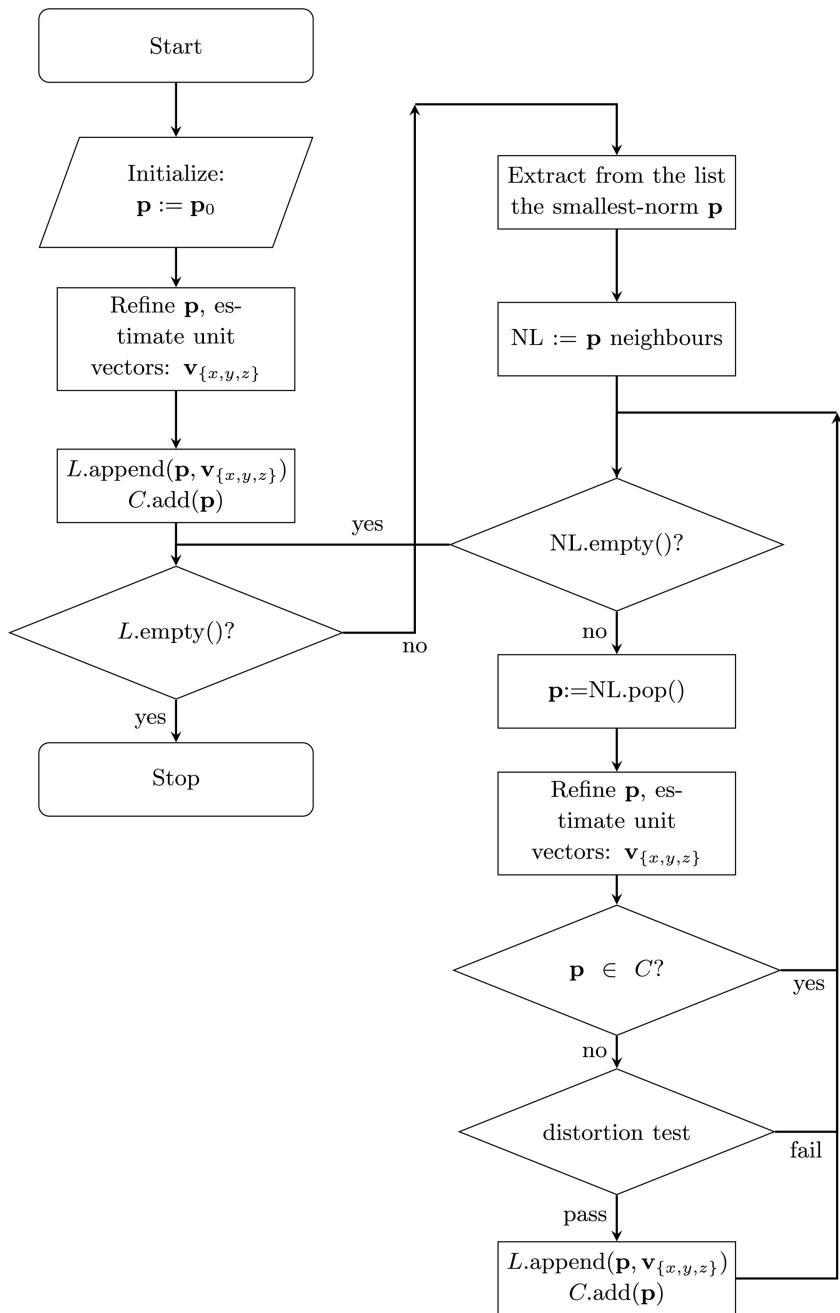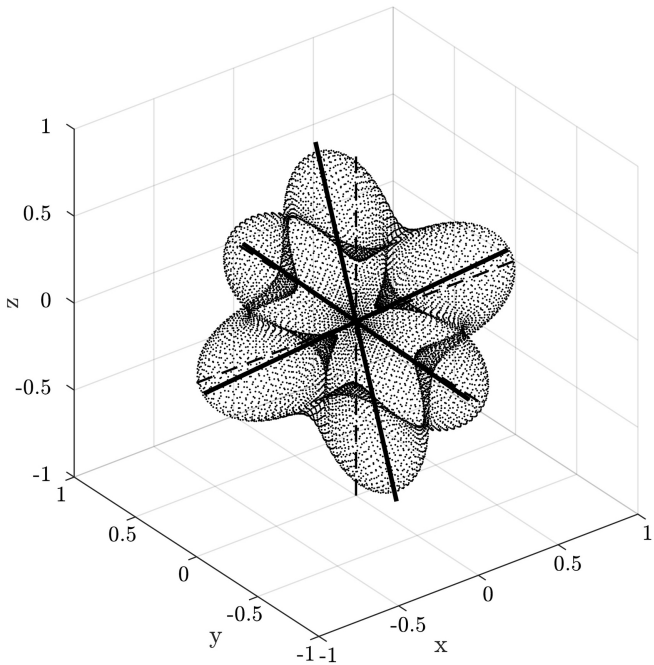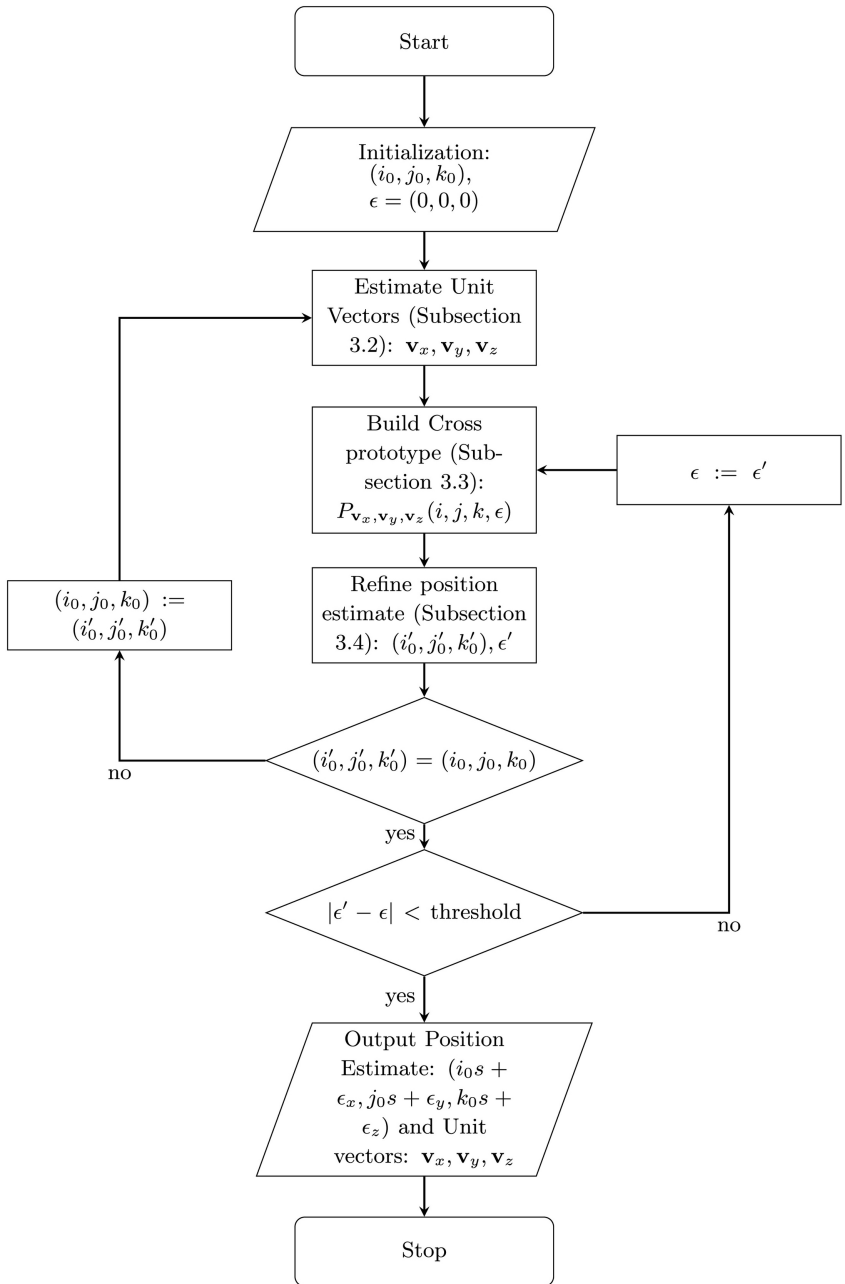(c) Simulated image (ZX) at isocentre

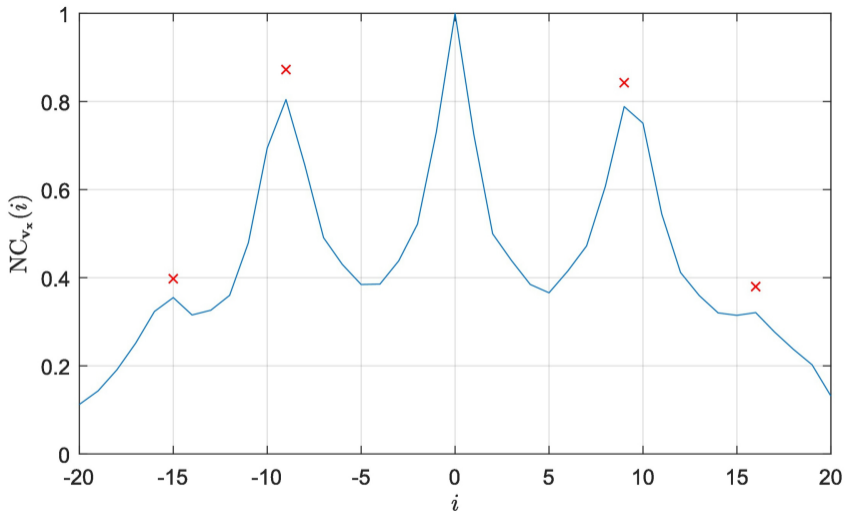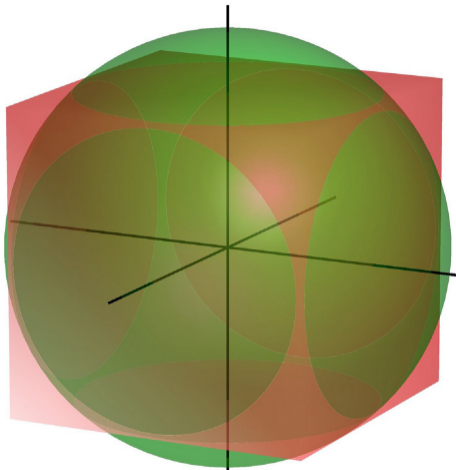(d) Simulated image (ZX) at 60 mm from isocentre

Figure 4

Figure 5

Figure 6

Figure 7

Figure 8

Figure 9